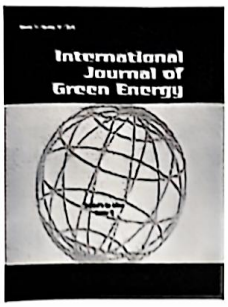

International Journal of Green Energy

ISSN: (Print) (Online) Journal homepage: www.tandfonline.com/journals/ljge20

Fast reconstruction of boiler numerical physical field based on proper orthogonal decomposition and conditional deep convolutional generative adversarial networks

Jiajian Long, Meirong Dong, Jieheng Zhou, Youcai Liang & Jidong Lu

To cite this article: Jiajian Long, Meirong Dong, Jieheng Zhou, Youcai Liang & Jidong Lu (2024) Fast reconstruction of boiler numerical physical field based on proper orthogonal decomposition and conditional deep convolutional generative adversarial networks, International Journal of Green Energy, 21:12, 2653-2671, DOI: 10.1080/15435075.2024.2322976

To link to this article: https://doi.org/10.1080/15435075.2024.2322976

Published online: 03 Mar 2024.

INTERNATIONAL JOURNAL OF GREEN ENERGY
2024, VOL. 21, NO. 12, 2653–2671
https://doi.org/10.1080/15435075.2024.2322976

Taylor & Francis
Taylor & Francis Group

Fast reconstruction of boiler numerical physical field based on proper orthogonal decomposition and conditional deep convolutional generative adversarial networks

Jiajian Long[a,b], Meirong Dong[a,b], Jieheng Zhou[a,b], Youcai Liang[a,b], and Jidong Lu[a,b]

[a]School of Electric Power, South China University of Technology, Guangzhou, Guangdong, China; [b]Guangdong Province Engineering Research Center of High Efficient and Low Pollution Energy Conversion, Guangzhou, Guangdong, China

ABSTRACT

Obtaining real-time physical field data inside the boiler furnace is crucial for combustion diagnostics and optimization. In this work, we propose a fast reconstruction technique for the physical fields in a tangentially-fired coal boiler. The method combines the Proper Orthogonal Decomposition (POD) and Conditional Deep Convolutional Generative Adversarial Networks (cDCGAN) based on the boiler physical field obtained by computational fluid dynamics (CFD). Firstly, CFD simulations are performed using data from the boiler Distributed Control System (DCS). After verifying the CFD results, we expanded the simulation to 105 operational condition cases sample sets. Then, the physical fields of the sample set undergo POD to determine the appropriate number of POD bases, thereby ensuring the accuracy of the reconstruction. Finally, the cDCGAN method is employed to establish the correlation between the POD bases and the operational conditions of the boiler. Results show that the POD-cDCGAN method achieves rapid and accurate reconstruction of temperature and velocity fields, with mean relative error (MRE) below 1.5% and root relative squared error (RRSE) below 5.7%. The reconstruction time is reduced to 10.57s, significantly faster than direct CFD methods. The POD-cDCGAN method offers an efficient approach for online operational diagnosis and digital twin construction of boiler equipment.

ARTICLE HISTORY
Received 5 December 2023
Accepted 20 February 2024

KEYWORDS
Boiler physical field; CFD; proper orthogonal decomposition(POD); cDCGAN; reduced order modeling

1. Introduction

With the growing global energy demand for energy and a growing emphasis on environmental sustainability, significant changes are occurring in the world's energy structure, especially regarding coal-fired power generation. However, coal-fired electricity still holds an important position, which offers stability and dispatchability advantages in the power system, making it capable of meeting peak load and frequency regulation requirements. Coal-fired boilers, as the core equipment in thermal power generation, play a crucial role in peak load regulation and frequency control. The boiler online operating conditions directly impact the overall performance of the power generation unit (Li et al. 2023; Meng et al. 2021; Ronquillo-Lomeli and García-Moreno 2024). The operating state of the boiler is closely related to the distribution of the combustion field in the furnace. The information found within the combustion field which includes temperature, pressure, and component concentrations can reflect the combustion status in the furnace (Qinghong 2020; Wang et al. 2019; Yu, Sang, and Sun 2020).

There are several methods available for obtaining the distribution of the physical field inside the boiler furnace, such as acoustic measurements (Modliński et al. 2015; Wang et al. 2021; Zhang et al. 2015), optical reconstruction [10–13] (Golgiyaz, Talu, and Onat 2019; Lou and Zhou 2005; Salinas et al. 2020; Yan et al. 2020), which requires the addition of measurement sensors. CFD is a technique that employs the finite volume method to iteratively calculate and obtain the physical field distribution of the boiler. The enhancement of computer processing capability and computational techniques has facilitated the utilization of CFD techniques in industrial procedures. These methods have been validated for accuracy, especially in the design analysis (Bianco et al. 2021; Crnomarkovic et al. 2020; Kang and Ding 2020; Purnomo et al. 2019; Zhan, Ding, and Zhuang 2020), optimization and retrofitting (Belosevic et al. 2009; Hao et al. 2020; Milićević et al. 2020; Yan et al. 2012; Zhou et al. 2020), and offline operation and maintenance diagnostics (Liu et al. 2022; Madejski et al. 2019; Mitchell et al. 2016; Purnomo et al. 2019; Sung et al. 2016; Wang, Zhang, and Liu 2020) of coal-fired power plants. However, these methods are still not widely used in the actual online operation of power plant boilers. The main reason is that the large computational workload and time-consuming iterations required by numerical simulations, which lack real-time performance and speed, making them unsuitable for meeting the demands of online equipment operation.

With the rapid expansion of artificial intelligence algorithms, many researchers combine artificial intelligence methods with numerical simulation methods to obtain the rapid computation of physical fields (Cao et al. 2023; Deng et al. 2019; Diederich, Di Bartolo, and Benim 2023). Artificial intelligence algorithms construct corresponding network models that sacrifice a certain level of accuracy while ensuring a certain level of computational accuracy, thereby significantly

CONTACT Meirong Dong epdongmr@scut.edu.cn School of Electric Power, South China University of Technology, 381 Wushan Road, Tianhe District, Guangzhou, Guangdong 510640, China

improving real-time performance and speed. Lee et al (Lee et al. 2021). and Park et al (Park, Lee, and Huh 2022). both constructed Reduced Order Models (ROM) using POD and Radial Basis Function Network (POD-RBFN) and created digital twins of boilers to reconstruct the temperature field based on the CFD data. However, both methods combined with RBFN suffer from significant reconstruction errors in high-gradient turbulent combustion zones. Jiang et al (Jiang et al. 2023). conducted CFD simulations to obtain the temperature field of the active cooling channel of hydrocarbon fuel. They proposed a ROM reduction model by combining POD with Autoencoder Neural Network (ANN) within the framework of a Kriging model. This model effectively addressed the temperature field reconstruction errors in high-gradient regions. It successfully reconstructed the temperature and velocity fields with reduced global error, achieving acceptable reconstruction accuracy. Sun et al (Sun et al. 2022). introduced Convolutional Autoencoder for fast two-dimensional temperature field reconstruction by inputting a small amount of sensor data. Due to its non-linear characteristics, it provides more accurate results compared to interpolation extrapolation and POD-RBFN. Wang et al (Wang, Chen, and Zhong 2024). obtained the distribution data of temperature and oxygen by CFD, innovatively combined POD with Support Vector Machine (SVM) for fast reconstruction and associated the reconstructed physical field with slagging distribution using fuzzy comprehensive evaluation, obtaining the occurrence and distribution of slagging on water-cooled walls. However, there were still significant errors in the scalar field in the local low O_2 value area. Moreover, the method of POD dimension reduction is widely used in fiber optics industry (Zhu and Ji 2023), transformer temperature simulations (Liu et al. 2024), and other fields, fully utilizing the dimension reduction characteristics of POD and combining them with artificial intelligence methods to quickly and accurately obtain the distribution of physical fields for online analysis and diagnostics.

There is significant potential for the application of POD and artificial intelligence algorithms in the field of physical field reconstruction. Deep Convolutional Generative Adversarial Networks (DCGAN) based on competitive strategy have demonstrated remarkable effectiveness in image processing. Radford et al (Radford, Metz, and Chintala 2015). first proposed DCGAN by combining CNN with GAN. Since then, DCGAN has been widely applied in various applications such as image generation (Patgiri, Biswas, and Roy 2021), image recognition (Dewi et al. 2022), and image restoration (Li et al. 2019). These applications highlight the strength of this model. However, it has not been used in physical field reconstruction. Building upon the DCGAN model, the addition of input conditions forms the cDCGAN, which leverages the generative capabilities of the DCGAN's deep neural network. This makes it applicable for generating physical fields under different operating conditions.

In order to further expand the application of physical field in the actual online operation of boilers, we propose a method for fast reconstruction of the physical field. In this work, we obtained the physical field distribution of the boiler under different operating conditions using CFD methods. These physical fields are generally classified into scalar fields and vector fields. Taking temperature and velocity fields as the representatives, the combined POD-cDCGAN method is suggested to rapidly reconstruct the physical field distribution within the boiler furnace. The reconstructed results are compared with those directly obtained from CFD. This technique aims to enable rapid, accurate reconstruction accuracy, while improving computational efficiency and real-time capability for on-site applications.

2. Methodology and materials

2.1. Research object

This work focuses on a 330 MW tangentially subcritical coal-fired boiler as the research object. The detailed information can be found from our previous work (Ye et al. 2022). Briefly, the burner injections of the boiler are arranged in a quadrangular pattern, with each corner consisting of 16 layers of burner injections. The lower group of burners includes AA, A, AB, B, BC, C, and CC injections. The middle group of burners includes DD, D, DE, E, and EE injections. The upper group of burners includes SOFA1, SOFA2, SOFA3, and SOFA4.

The simplified geometric structure of the boiler is shown in Figure 1, including the geometric model (Figure 1 (a)) and the mesh model (Figure 1 (b)). The boiler burner area is the region with the most intense turbulent combustion, and the mesh is refined in this area (Figure 1 (c)). CFD simulation is conducted for the combustion in the furnace of the boiler, using the numerical model listed in the following Table 1.

Based on the boiler's geometric dimensions, the geometric and mesh models were constructed using ICEM 19.2 software. The constructed mesh model was then used for boiler numerical simulations using Fluent 19.2 software. To ensure that the calculation results remain unaffected by the number of grids used, it is essential to carry out a mesh independence test, as Figure 2. By comparing facet average temperature values at different heights using various grid number, a mesh model comprising of 9.85×10^5 cells has been selected to satisfy the requirements for computational speed and accuracy.

2.2. POD method

Proper Orthogonal Decomposition (POD) is a method used to extract the characteristic information from discrete data. It allows for the description and approximation of high-dimensional random processes using low-dimensional approximations. By representing complex physical field distributions through the superposition of multiple low-dimensional orthogonal basis functions, POD enables rapid reconstruction of the physical field distribution. This approach facilitates the simplification and approximation of the complex physical field, ultimately achieving the goal of efficient field reconstruction.

A field can be represented using a field function $u(x)$, as shown in Equation (1).

$$u = u(x) \tag{1}$$

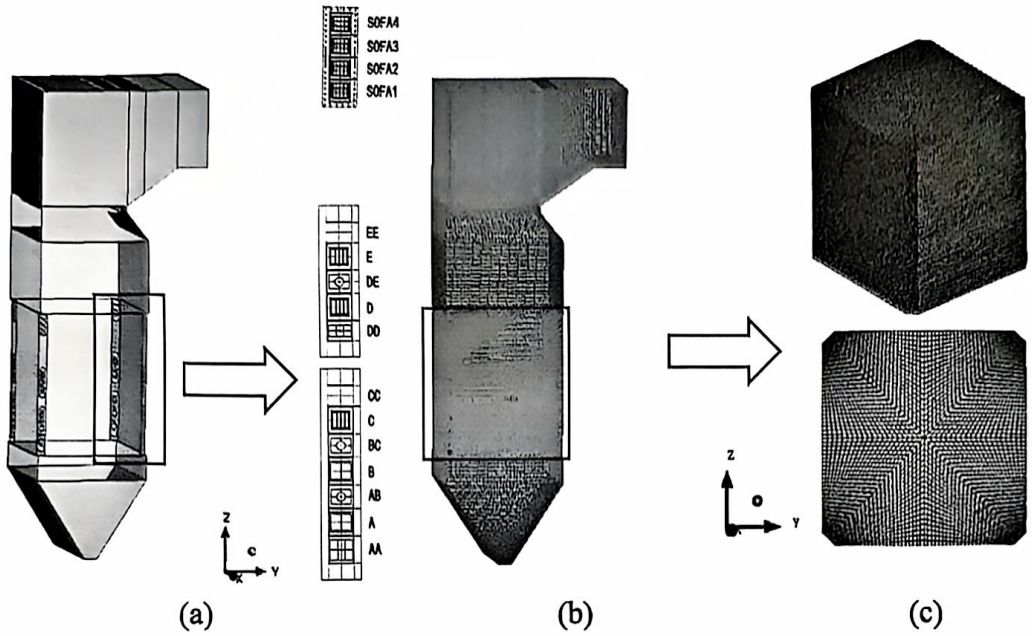

Figure 1. Tangential boiler structure: (a) tangential boiler geometric modeling; (b) tangential boiler meshing; (c) boiler burner area meshing and refinement.

Table 1. The main physicochemical phenomena and models of coal combustion (Ye et al. 2022).

Physicochemical process	Mathematic model
Gas phase turbulence	Realizable k-ε turbulence model
Particle orbit	Random orbit tracking model
Volatilization extraction	Dual competitive reaction pyrolysis model
Volatile combustion	Unpremixed combustion model
Coke burning	Dynamic/diffusion combustion model
Radiative heat transfer	*p*-1 radiation model
NOx model	Fuel type NOx, thermal type NOx

According to the polynomial decomposition of the function, the field function can be described using multiple basis functions.

$$u_N(x) = \sum_{j=1}^{N} a_j \varphi_j(x) \left\{ \varphi_j(x) \right\}_{j=1}^{\infty} \in L^2 \tag{2}$$

In the given equation, $u_N(x)$ can represent either a collection of physical field data obtained from multiple independent experiments or a collection of time-varying physical field data.

$$\begin{cases} u_N(x) = \{u^k\} \\ u_N(x) = u(x, t_k) \end{cases} \tag{3}$$

To ensure that the approximate solution obtained by using multiple basis functions to describe the field function is sufficiently reliable and accurate, it is necessary to minimize the average error between the field collection $u_N(x)$ and its projection onto the selected set of basis vectors φ_j, given by $\left(\frac{(u,\varphi)}{\varphi^2}\varphi\right)$.

$$\min_{\varphi \in \mathcal{H}} \left\langle \left\| u - \frac{(u,\varphi)}{\|\varphi\|^2} \right\|^2 \right\rangle \tag{4}$$

where the symbol $\|\cdot\|$ denotes the norm, specifically $f = (f,f)^{\frac{1}{2}}$; the notation $\langle \cdot \rangle$ represents taking the average; the symbol $\mathcal{H}$ represents the Hilbert space.

The given equation is equivalent to maximizing the projection of $u_N(x)$ onto the selected set of basis vectors φ_j, as shown in Equation (5).

$$\max_{\varphi \in \mathcal{H}} \frac{\langle |(u,\varphi)| \rangle^2}{\|\varphi\|^2} \tag{5}$$

The key to solving the equation is to compute the extremum of $|(u,\varphi)|^2$, which involves solving a variational problem subject to the constraint $\|\varphi\|^2 \leq 1 (\varphi \in \mathcal{H})$.
The variational problem functional can be represented by the following Equation (6).

Table 2. Hyperparameters table.

NO.	Hyperparameters	Parameter Description	Value
1	batch_size	Number of training batches: The total number of groups into which all training samples are randomly divided.	10
2	β1	Exponential decay rate for first-moment estimation: Controls the direction of model updates (gradients).	0.5
3	β2	Exponential decay rate for second-moment estimation: Controls the step size of model updates.	0.99
4	nc	Number of training image channels: Typically set as RGB (three channels).	3
5	nz	Size of the initial random matrix.	128
6	ngf	Size of the feature distribution map outputted by the generator.	128
7	ndf	Size of the original image samples inputted to the discriminator.	128
8	Learning_rate	Learning rate: Influences the model's robustness and affects the step size during optimization.	0.0002

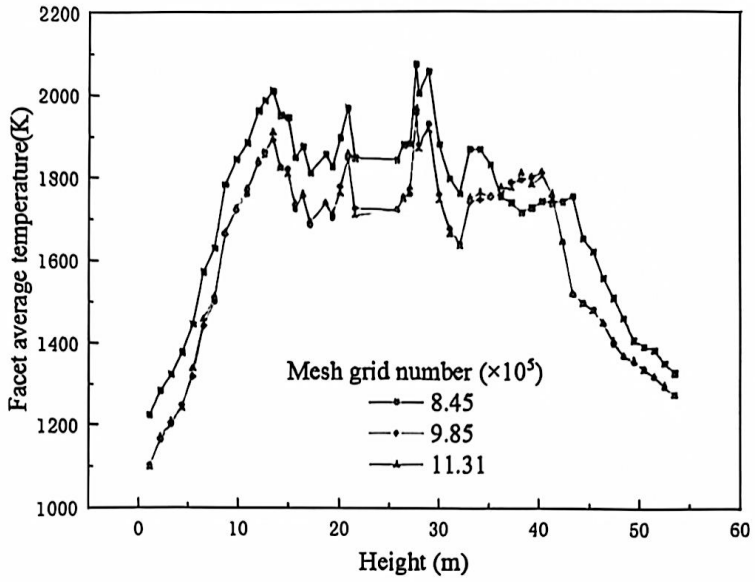

Figure 2. Mesh grid independence verification.

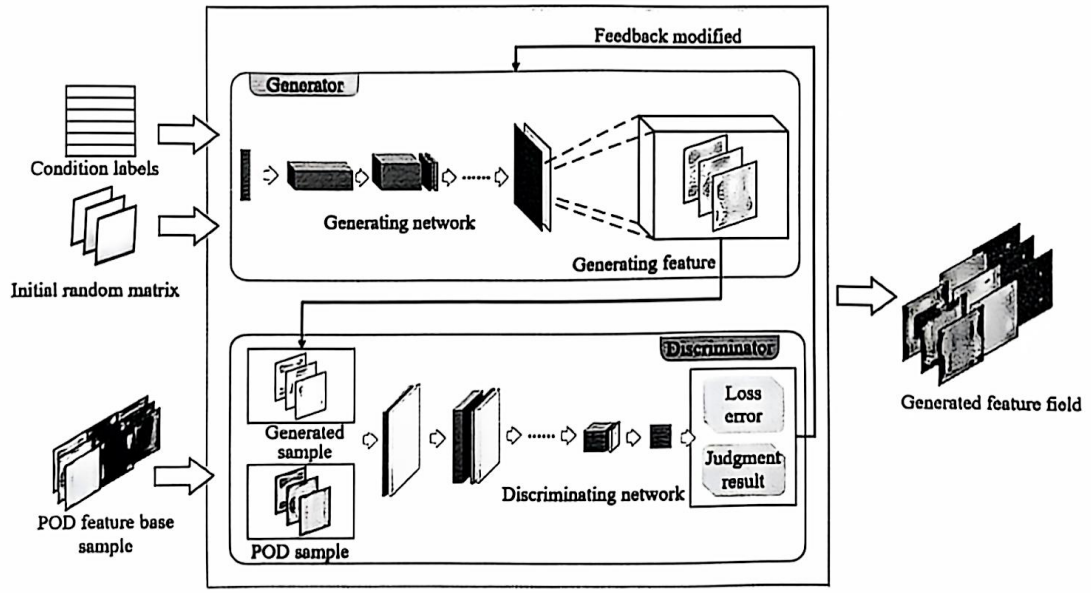

Figure 3. cDCGAN structure.

$$J[\varphi] = \langle |(u,\varphi)|^2 \rangle - \lambda\left(||\varphi||^2 - 1\right) \tag{6}$$

The necessary condition for attaining an extremum is that the derivative of the functional with respect to any variation ($\varphi + \delta\psi \in \mathcal{H}, \delta \in \mathbb{R}$) is equal to zero.

$$\begin{aligned} \frac{d}{d\delta} J[\varphi + \delta\psi]\Big|_{\delta\to 0} &= 0, \\ &= \frac{d}{d\delta}\left[\langle (u, \varphi + \delta\psi)(\varphi + \delta\psi, u)\rangle - \lambda(\varphi + \delta\psi, \varphi + \delta\psi)\right]\Big|_{\delta\to 0}, \\ &= 2Re[\langle (u,\psi)(\varphi,u)\rangle - \lambda(\varphi,\psi)] = 0 \end{aligned} \tag{7}$$

Re represents the real part of a complex number. By exchanging the averaging operation and inner product, the expression within the brackets in the given equation can be simplified to Equation (8).

$$\langle (\varphi,u)u,\psi\rangle - \lambda(\varphi,\psi) = 0, \Rightarrow (\mathcal{R}\varphi - \lambda\varphi,\psi) = 0 \tag{8}$$

$\mathcal{R}$ is a linear operator defined as $\mathcal{R}\varphi = (\varphi,u)u$. Since ψ is an arbitrary variation, the given equation is equivalent to solving an eigenvalue problem, which transforms the original extremum problem into an eigenvalue problem.

$$\Rightarrow \mathcal{R}\varphi = \lambda\varphi \tag{9}$$

Therefore, the linear operator $\mathcal{R}$ can also be understood as the optimal basis for the field collection u, given by the

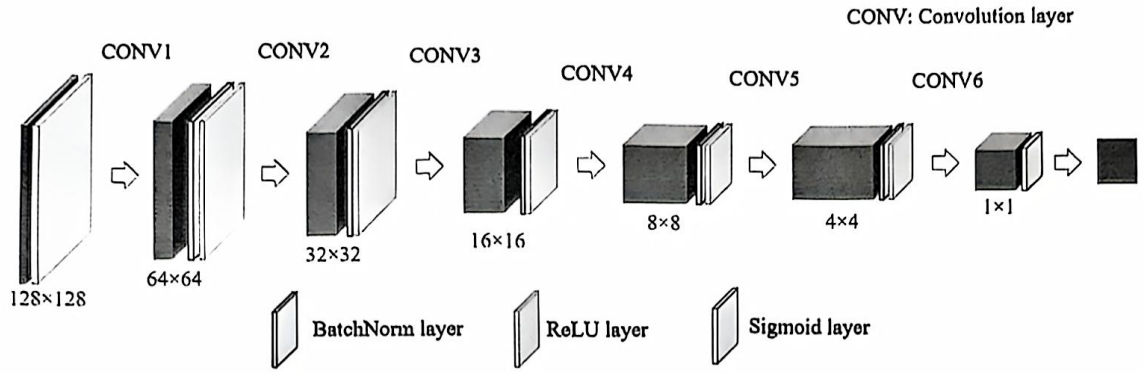

Figure 4. Discriminator network structure diagram.

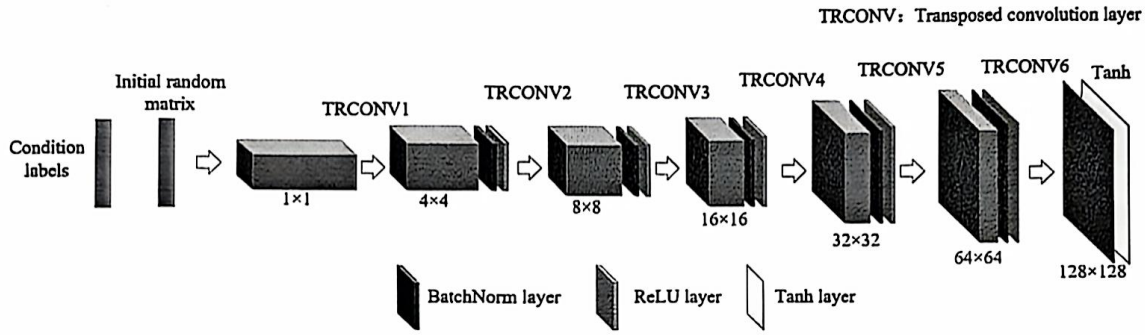

Figure 5. Generator network structure diagram.

eigenfunctions $\varphi_j(x)$. This optimal basis characterizes the field function through a linear relationship.

In the decomposition, the contribution of each mode to the overall decomposition is quantified by its corresponding eigenvalue, which is referred to as the mode energy. This parameter can be used to quantitatively measure the effectiveness of the mode decomposition and analyze the degree of influence brought by each mode.

The mode energy is evaluated based on the eigenvalues corresponding to each mode's orthogonal basis. The energy of the n^{th} mode, denoted as ξ_n, can be defined as shown in Equation (10).

$$\xi_n = \lambda_n / \sum_{n=1}^{N} \lambda_n \tag{10}$$

2.3. cDCGAN algorithm

When constructing the relationship between operating condition parameters and the modal characteristics of the physical field, by considering the operating condition parameters as conditions, adding a conditional label in front of the DCGAN network serves as an identifier. This approach, known as condition-DCGAN (or cDCGAN for short), enables the generation of physical field modal characteristics conditioned on the operating condition parameters (Qian and Liu 2022; Zhong et al. 2019). As shown in Figure 3, it shows the cDCGAN network structure used in this paper.

The discriminator target is shown in Equation (11).

$$\max_D V(D,G) = E_{x\sim pdata(x)}[logD(x)] + E_{z\sim pz(z)}[\log(1 - D(G(z)))] \tag{11}$$

For the discriminator network D^*, as shown in Figure 4, its objective is to maximize the output probability $D(x)$ for real samples and minimize the output probability $D(G(z))$ for generated samples. This is equivalent to maximizing $1 - D(G(z))$ since the goal is to make the discriminator distinguish generated samples as fake (assigning them low probability). Therefore, for the discriminator network, the objective is to maximize the loss function, denoted as $\max_D V(D,G)$ (Sha et al. 2023; Zhong et al. 2020).

The generator target is shown in Equations (12), (13).

$$\max_G V(D,G) = E_{z\sim pz(z)}[log(D(G(z)))] \tag{12}$$

$$\min_G V(D,G) = E_{z\sim pz(z)}[log(1 - D(G(z)))] \tag{13}$$

The objective of the generator network G^* is to generate outputs that closely resemble real samples and possess the ability to accurately predict outputs based on input conditions. Therefore, the generator aims to maximize the probability that the discriminator network assigns to its generated samples, denoted as $D(G(z))$. This is equivalent to minimizing $1 - D(G(z))$, as a smaller value indicates a higher probability

of the generated sample being classified as real by the discriminator network (Sha et al. 2023; Zhong et al. 2020). The generator network structure is shown in Figure 5.

By combining the objectives of the discriminator network and the generator network, we can derive the overall optimization objective for the entire loss function.

The overall goal is shown in Equation (14)

$$\min_G \max_D V(D,G) = E_{x\sim pdata(x)}[logD(x)] + E_{z\sim pz(z)}[\log(1-D(G(z)))] \quad (14)$$

According to the overall objective, the training process involves training the discriminator network and the generator network to obtain the optimal network parameters (Rajabi et al. 2023). The training hyperparameters are shown in Table 2.

The loss function utilized in this study is binary cross-entropy, as shown in Equations (15) and (16). It serves as a measure of the deviation between the output results and the expected values at each iteration step, guiding the training in the direction of reducing the deviation.

$$loss = \frac{1}{N}\sum_{n=1}^{N} l_n \quad (15)$$

$$l_n = -w[y_n \cdot logx_n + (1-y_n)\cdot log(1-x_n)] \quad (16)$$

where l_n represents the loss function of sample n; y_n denotes the label of sample n; 1 represents the positive class and 0 represents the negative class; x_n represents the probability of sample n being predicted as the positive class.

2.4. Model evaluation

The grid point value errors of the field fast reconstruction using the combined POD-cDCGAN method are generally analyzed quantitatively using mean relative error (MRE) and root relative squared error (RRSE), as shown in Equations (17) and (18), respectively.

$$\mathrm{MRE} = \frac{1}{N}\sum_{n=1}^{N}\frac{\left(\varphi_{POD-cDCGAN,I} - \varphi_{CFD,I}\right)}{\varphi_{CFD,I}} \times 100\% \quad (17)$$

$$RRSE = \sqrt{\frac{\sum_{n=1}^{N}\left[\left(\varphi_{POD-cDCGAN,I} - \varphi_{CFD,I}\right)/\varphi_{CFD,I}\right]^2}{N}} \times 100\% \quad (18)$$

where N is the number of grid points in the compared physical field, $\varphi_{POD-cDCGAN,I}$ is the parameter value generated by the POD-cDCGAN on the current grid point, and $\varphi_{CFD,I}$ is the parameter value obtained through CFD numerical simulation on the current grid point.

3. Results and discussions

3.1. CFD result verification

Four typical load conditions of the actual boiler operation are selected for simulation and experimental calculations. The operational parameters for each condition are shown in Table 3. The proximate and elemental analysis of coal are shown in Table 4.

Using the standard pressure difference scheme and adopting a second-order upwind accuracy scheme for the convection term, the calculations are performed until the residuals of each equation are smaller than 1×10^{-3}, indicating convergence of the simulation results. Based on the converged results, a conservation verification and an error verification between the simulation and measurement points are conducted.

Figure 6 presents CFD result conservation verification. It can be observed that the numerical simulation results of the boiler exhibit mass conservation between the input and output

Table 3. Verification operating condition parameter table.

Boiler operating condition	Load 1	Load 2	Load 3	Load 4
Boiler load(%)	69.8	71.98	74.55	84.07
Coal feed rate of coal feeder A (kg/s)	27.87	32.17	29.93	29.30
Coal feed rate of coal feeder B (kg/s)	27.83	29.66	29.94	35.44
Coal feed rate of coal feeder C (kg/s)	26.18	33.02	25.01	36.59
Coal feed rate of coal feeder D (kg/s)	27.18	29.55	30.04	33.56
Coal feed rate of coal feeder E (kg/s)	−0.05	1.24	−0.05	−0.06
Total primary air volume (Nm3/h)	258.63	272.61	282.16	313.17
Total secondary air volume (Nm3/h)	458.76	442.60	488.64	580.51
A inlet air volume (Nm3/h)	48.39	52.29	56.87	57.14
B inlet air volume (Nm3/h)	51.25	52.05	56.02	56.34
C inlet air volume (Nm3/h)	55.52	53.36	53.69	56.63
D inlet air volume (Nm3/h)	50.45	52.62	51.72	51.58
E inlet air volume (Nm3/h)	0.05	0.06	0.08	0.03

Table 4. Properties of coal of typical operating condition.

	Proximate analysis(%,ar)					Ultimate analysis(%,ar)				
Condition	M_{ar}	A_{ar}	V_{ar}	$F_{c,ar}$	$Q_{ar,net}$ (MJ/kg)	C_{ar}	H_{ar}	O_{ar}	N_{ar}	S_{ar}
Load 1	17.12	13.35	25.27	44.26	19.66	49.98	4.43	13.53	1.03	0.56
Load 2	16.56	14.99	25.09	43.36	20.75	55.90	2.95	8.03	1.02	0.56
Load 3	16.18	19.26	23.45	41.11	19.51	50.25	3.74	9.24	0.96	0.37
Load 4	15.68	17.59	24.18	42.55	19.14	51.43	3.00	10.18	0.99	1.14

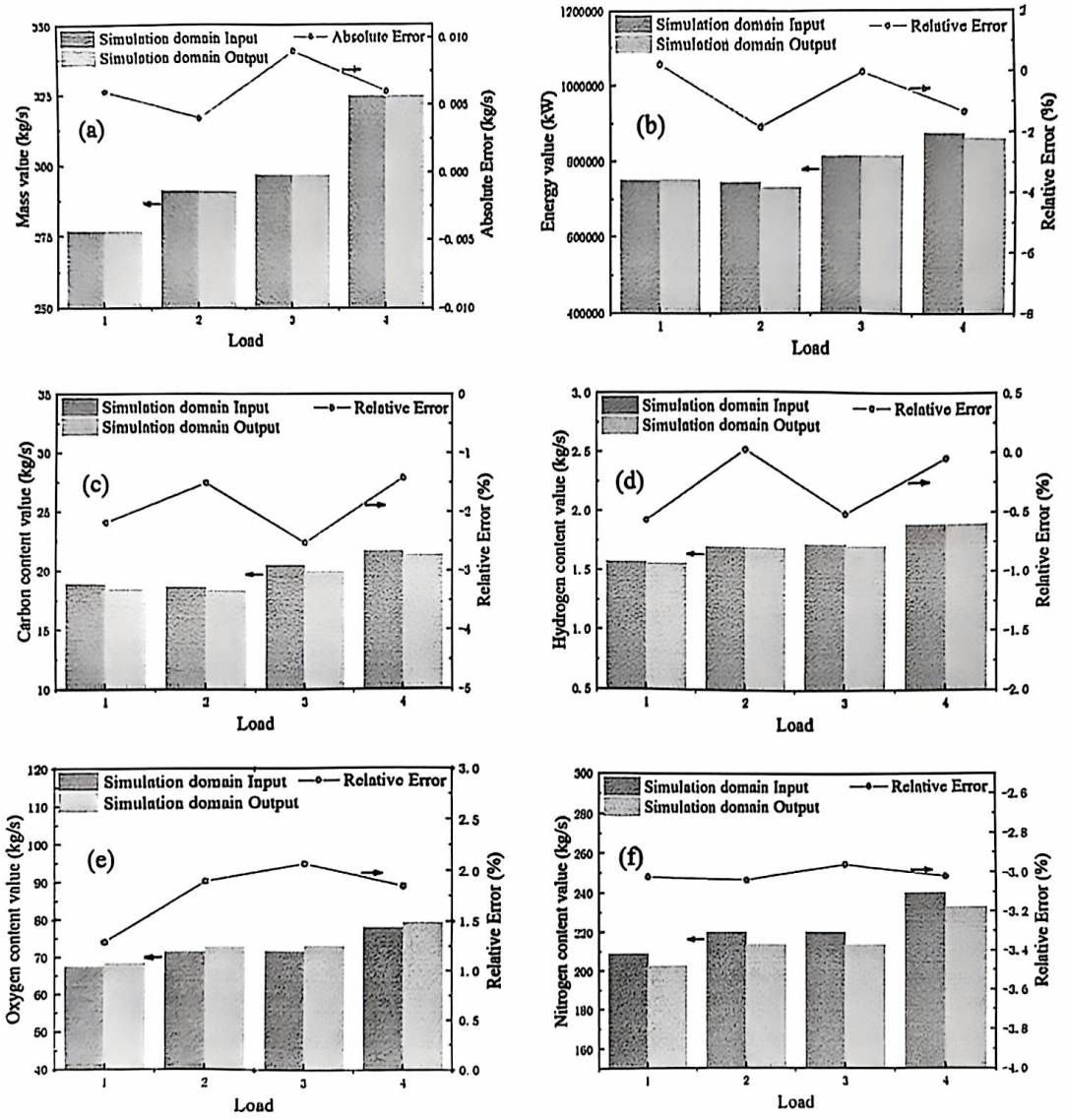

Figure 6. Numerical simulation results conservation verification: (a)Mass conservation; (b) energy conservation; (c) carbon content conservation; (d) hydrogen content conservation; (e) oxygen content conservation; (f) nitrogen content conservation.

of the computational domain, with minimal errors. In terms of energy input and output, the calculated deviation does not exceed 1.86%, which is in good agreement with the energy conservation at the inlet and outlet of the computational domain. The main elemental conservation in the numerical simulation of boiler combustion includes C, H, O, and N. The simulation results show that the mass conservation of these elemental components between the input and output of the computational domain is well-maintained, with a calculated deviation not exceeding 3.04%. Based on the above analysis, it can be concluded that the numerical simulation results of the boiler satisfy the conservation laws, and the simulation results are both convergent and reliable.

Figure 7 presents the error verification results between the simulation and measurement points, providing the consistency between the numerical simulation of the boiler and its practical operation. At the outlet of the reheater, the error between the measured flue gas temperature and the simulated average surface temperature does not exceed 2.865%. Regarding the NOx emission, which is related to combustion, the error between the measured concentration point and the simulated average result does not exceed 3.858%. Therefore, it can be concluded that the numerical simulation of the boiler is consistent with the actual boiler operation, exhibiting consistency and accuracy.

After evaluating the outlet parameters against actual measurements for various operating conditions of the boiler, and conducting three conservation checks, it can be concluded that the numerical model for boiler simulation is reliable and accurate. Utilizing this numerical model, a large number of numerical simulations are performed using historical operational data from the power plant. As shown in Figure 8, a comparison is made between the prediction errors and computational cost for different numbers of cases. In order to achieve a good balance between computational accuracy and cost, we select

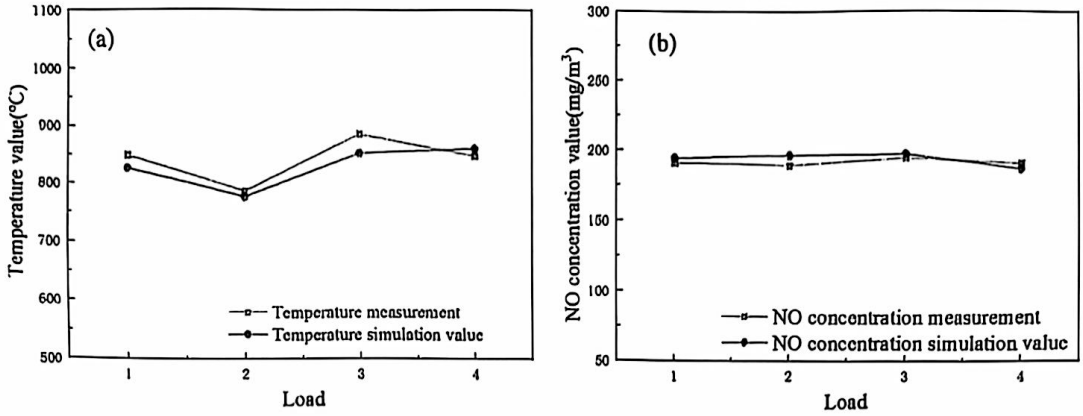

Figure 7. Furnace outlet flue gas parameter verification: (a) temperature value comparison; (b) NO value comparison.

a total of 105 cases, where the average RRSE at this point is below 5%.

Subsequently, the simulated data samples are utilized to train the POD-cDCGAN model. The POD spatial field decomposition is carried out based on the appropriate sample size this sample, and the cDCGAN network model is constructed using the decomposed POD basis functions.

3.2. Proper orthogonal decomposition result

3.2.1. Physical field decomposition analysis

Figure 9 (a, b, c and d) present the temperature, velocity, oxygen and carbon monoxide field of CFD sample, with Load 3 (74.55%) in Table 3 as an example. The cross-sections (x = 0) of the temperature field and velocity field exhibit an "A" shaped distribution, demonstrating good left-right symmetry. In the temperature field (Figure 9(a)), the central low-temperature region of each injection layer gradually shrinks from the bottom to the top, while the high-temperature regions connect and form a continuous area with increasing height. This indicates that in the boiler burner area, as the coal powder and airflow spiral upwards, there is continuous combustion and heat release. The combustion becomes most intense as it reaches the flame core in the middle and upper burner sections. In the velocity field (Figure 9(b)), high-speed areas are observed at the four corner inflow streams. The high-speed airflow carries the coal powder into the center of the furnace, forming four inflow streams that are tangential to the hypothetical circular design. Then, as the flow moves downstream, it diffuses and forms well-defined circular patterns in the furnace center.

The oxygen concentration field and carbon monoxide field (Figure 9(c) & (d)) exhibit opposite distributions. In the furnace, air is injected through the injections. This creates an oxygen-rich environment in the four corner airflow regions. The oxygen-rich environment promotes the devolatilization and combustion of coal powder. As a result, a significant amount of oxygen is consumed in the process. As the airflow entrains coal powder into the middle of the furnace, the coal

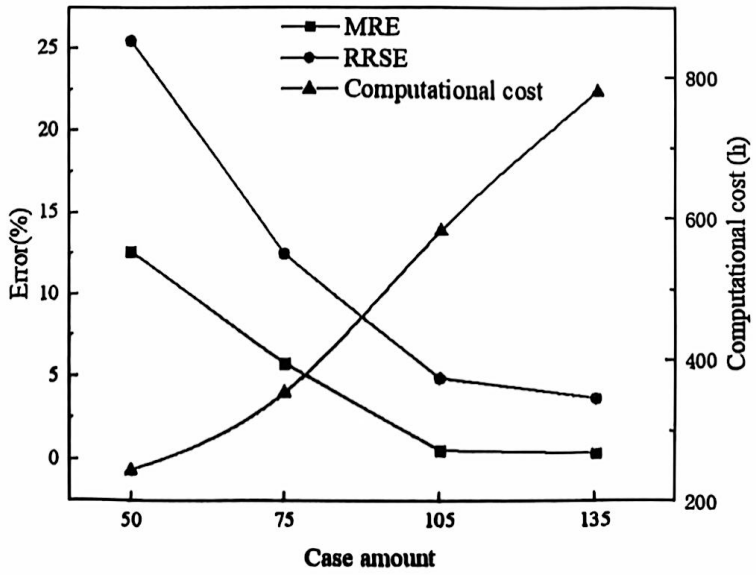

Figure 8. The errors and computational cost of different case amounts.

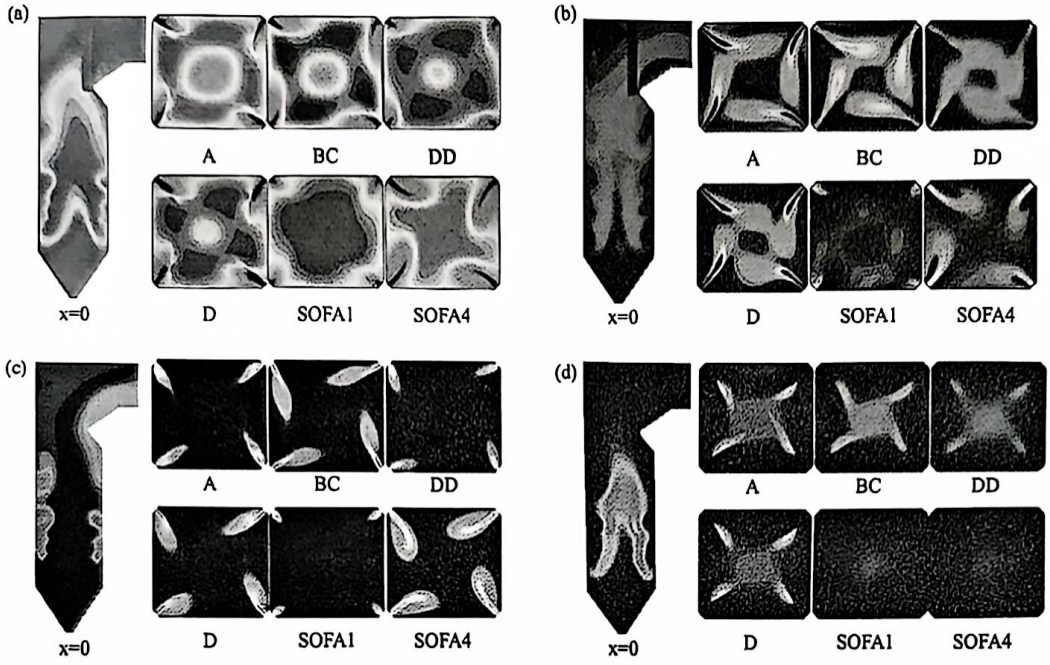

Figure 9. CFD physical field: (a) temperature field distribution; (b) velocity field distribution; (c) oxygen field distribution; (d) carbon monoxide field distribution.

powder undergoes combustion under oxygen-deficient conditions, resulting in the formation of a large amount of carbon monoxide in the central region of the furnace. As the airflow spirals upward, the coal powder-laden flow reaches the SOFA layer, where a substantial amount of air enters. This further promotes the combustion of incompletely burned coal powder and carbon monoxide. As a result, carbon monoxide starts to decrease sharply in the SOFA1 layer, while the entry of air significantly increases the oxygen concentration. The flue gas continues to flow into the horizontal flue gas duct.

Temperature and velocity fields can be represented as scalar and vector fields, respectively, and can be decomposed into their respective components.

The boiler burner area of the boiler numerical simulation samples is subjected to POD decomposition, as shown in Figure 10. The modal distribution maps for the first three modes, the fifth mode, and the tenth mode are presented. The modal distribution maps for the first two modes exhibit a basic symmetric structure, with a distinct central low-temperature region. This signifies the presence of a central low-temperature structure in the original temperature field distribution. As the height increases, the circular distribution of the original temperature field becomes smaller, resulting in a reduction in the size of the low-temperature region in the first two modes. In the first mode, the four local high-temperature structures gradually approach and connect with each other.

The third mode exhibits an approximate central symmetric structure, with high-temperature structures near the wall. This reflects the presence of high-temperature peaks near the wall in the original physical field. As the height increases, the four high-temperature peaks in the original temperature field become more prominent and have higher values, corresponding to larger areas and values of the high-temperature structures in the third mode. Modes above the third mode tend to be similar. Taking the fifth mode and the tenth mode as examples, they exhibit a stripe-like distribution in the transverse direction. Their role is to adjust and correct the detailed parts of the previous key modes, making the reconstructed temperature field closer to the original temperature field.

Figure 11 displays the modal distribution of the velocity field found in the boiler burner area of the boiler numerical simulation samples. The original field exhibits four groups of incoming flows, forming a clockwise rotating vortex with a low-speed region at the center in a circular shape. The first mode exhibits a distinct low-speed region at the center, formed by a high-speed segment that approximates a rectangular shape. This corresponds to the characteristic morphological structure of the rear portion of the incoming flow in the original velocity field. As the height increases, the circular distribution of the original velocity field becomes smaller, leading to a reduction in the size of the low-speed region in the mode. The second and third modes exhibit multiple clusters of strip-like high-speed distributions, carrying the characteristics of the initial and rear segments of the incoming flow in the original velocity field.

Modes above the third mode exhibit similarities and show a stripe-like distribution in the transverse direction. Their role is to modify and supplement the key modes, capturing the detailed parts of the morphological structures of the incoming flow from the initial to the rear segments.

3.2.2. *Optimal number of orthogonal bases*

According to Equation (10), the modal energy of each mode is calculated to measure the contribution of each mode to modal decomposition, as shown in Figure 12. With an increasing mode order, the mode energy decreases rapidly and starts to level off around the order of 10.

Table 5 presents the cumulative energy values for POD modes with orders of 1, 2, 3, 5, 10, 15, and 20. As more modes are accumulated, the proportion of mode energy increases. When

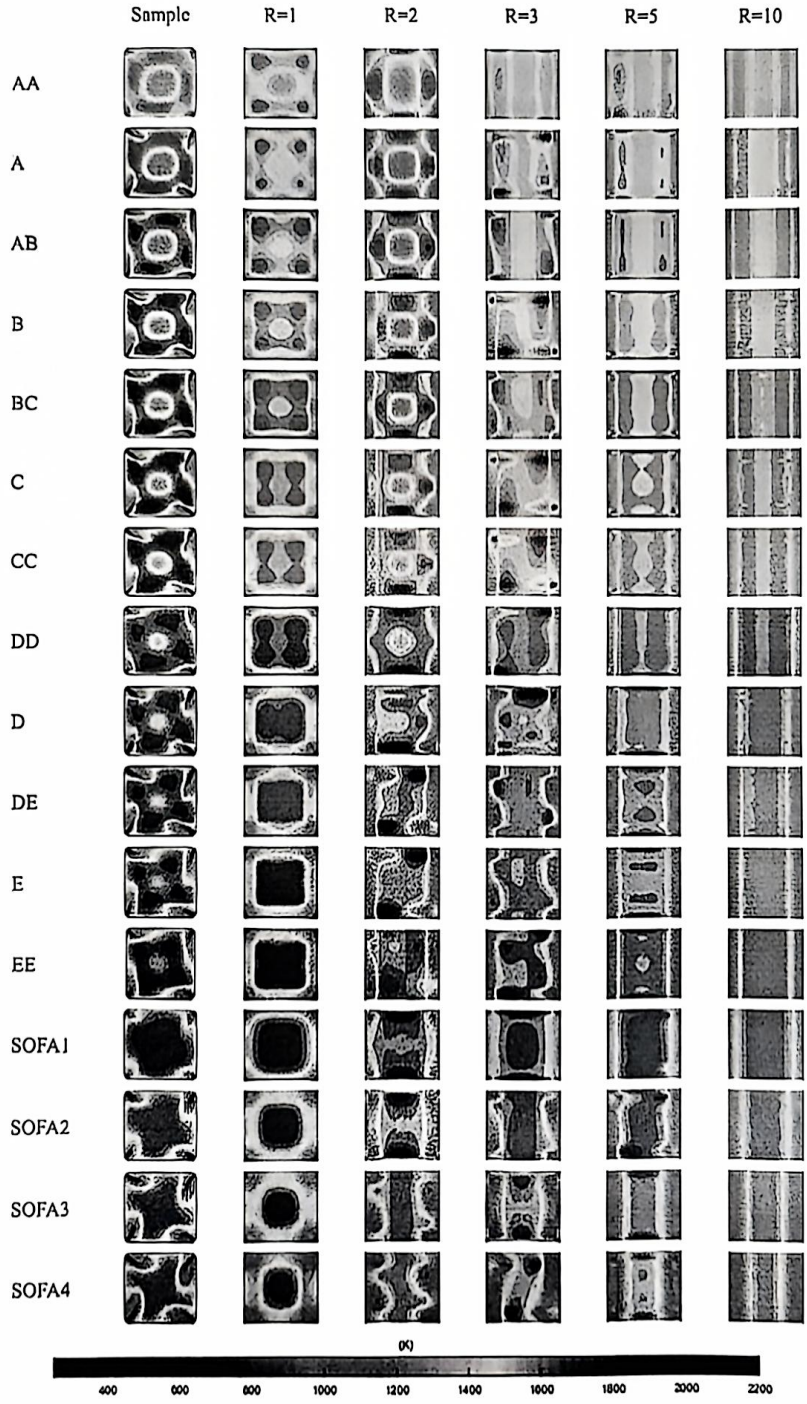

Figure 10. POD decomposition diagram of temperature field of burner nozzle section.

the mode order M is 5, the cumulative average mode energy does not exceed 81%. With an increasing mode order, the cumulative mode energy noticeably increases. At 10th order, the cumulative average mode energy reaches over 85%. Beyond the 10th order, the increase in cumulative energy diminishes. This corresponds to the energy distribution depicted in Figure 12, where at the 15th order, the cumulative average mode energy exceeds 93%, and at the 20th order, it accumulates to over 97%.

To achieve accuracy and speed, it is essential to carefully select the appropriate number of POD modes. The objective is to achieve a balance that allows for swift reconstruction of the physical field distribution while upholding the desired level of accuracy. The selection of 15 modes of POD bases, based on a thorough evaluation, is preferred because its energy accumulation is above 93%, and the number of modes is reasonable, thereby not affect the calculation speed.

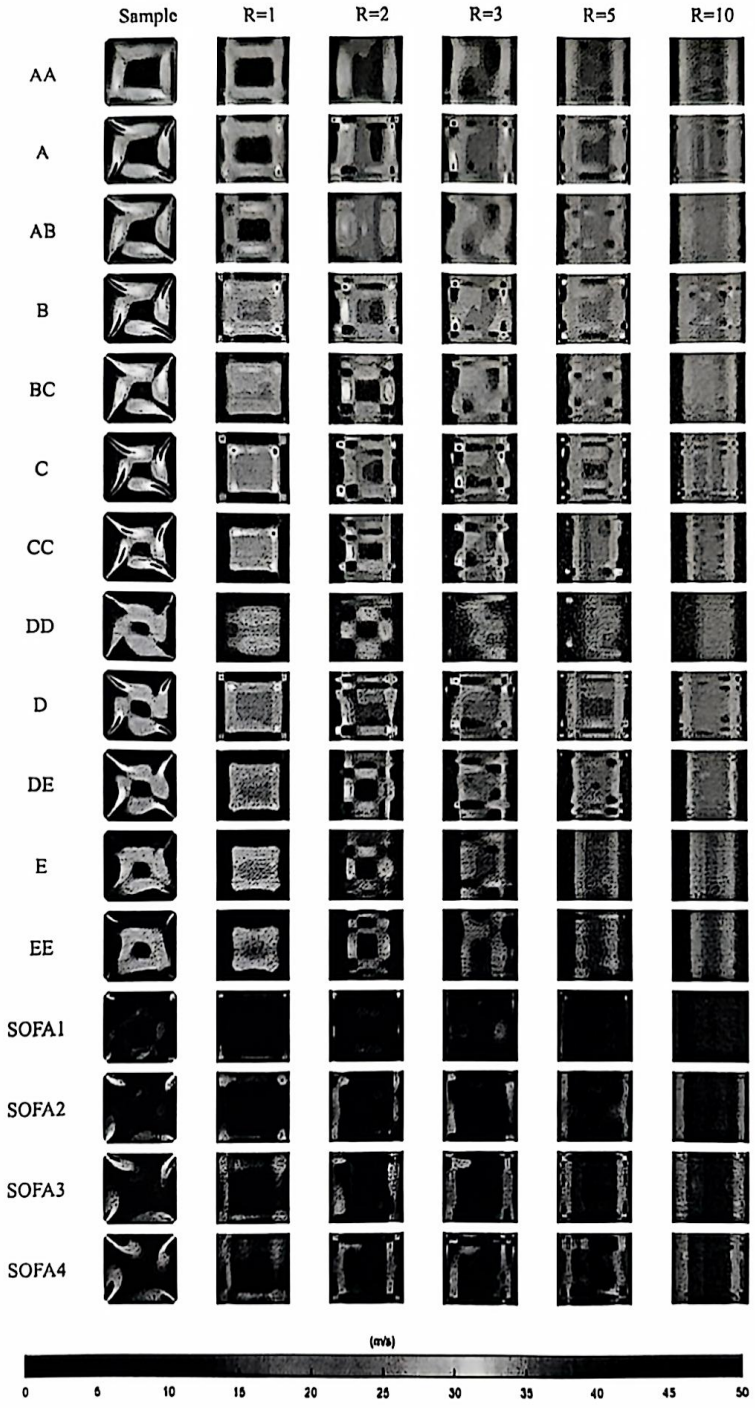

Figure 11. POD decomposition diagram of velocity field of burner nozzle section.

3.3. Construction of cDCGAN model

3.3.1. Model condition tag

In the construction of the relationship between operating parameters and POD modes, the operating parameters serve as conditional labels for the input of the generative adversarial network. They are combined with the initial random matrix as the training input parameters for the generative network. Through iterative training, feedback, and optimization, a network model representing the correlation between operating parameters and corresponding POD modes is obtained. The selection and classification of the operating parameters as important input labels have an impact on the convergence and accuracy of the correlation network model.

The output side of the correlation network model consists of the POD mode feature distribution related to the physical field of boiler combustion. On the input side, historical

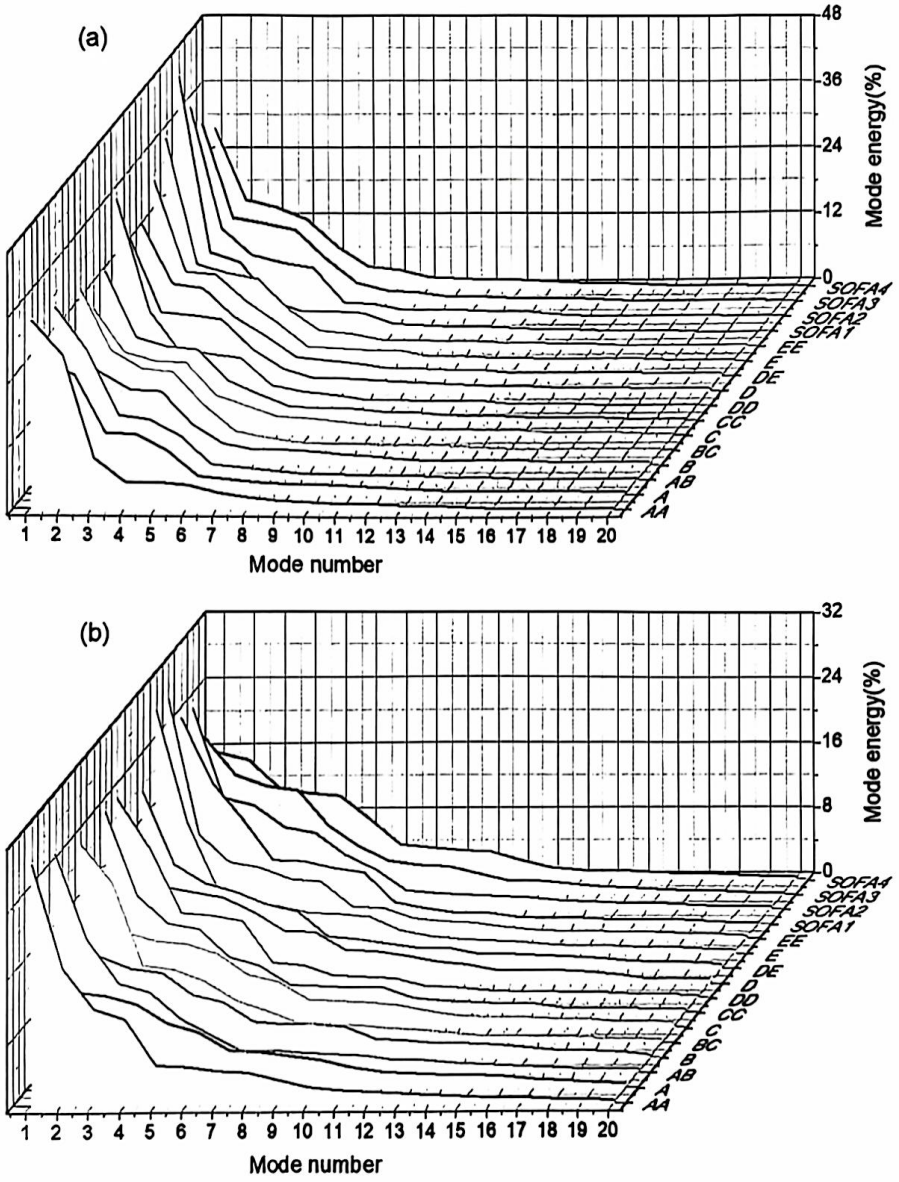

Figure 12. Energy distribution trends of the physical field decomposition in boiler burner area: (a) temperature field; (b) velocity field.

Table 5. Accumulated POD mode energy.

Mode number	Mode 1	Mode 2	Mode 3	Mode 5	Mode 10	Mode 15	Mode 20
Temperature	31.19	48.70	61.74	80.09	91.51	95.82	97.59
Velocity	22.87	37.74	48.87	66.74	86.59	93.85	97.03

operating parameters of the boiler equipment are used to train the model. For coal combustion, the differences in coal types significantly affect the combustion distribution. In particular, the fix carbon, volatiles, ash, and moisture in coal greatly influence the combustion rate and combustion temperature in the furnace. The coal quantity and air volume entering the burner affect the intensity of coal combustion and the combustion temperature inside the furnace, resulting in different boiler load outputs. The angle of the injections influences the angle of the coal particle injection flow, thereby causing variations in the height and angle of combustion distribution inside the furnace, directly impacting the distribution of physical fields. Therefore, the coal type, coal quantity, air quantity, and injection angle are selected as the primary input parameters. As shown in Table 6, these parameters serve as inputs for the furnace boundary, determining the distribution of the combustion physical field inside the furnace.

3.3.2. Model training

The cDCGAN algorithm network was constructed using the Python 3.6.1 programming language in the Spyder programming software. The network model construction involved building the generator network and discriminator network.

Table 6. Combustion input feature parameters for operating conditions.

Combustion Input Feature Parameters					
Coal type	Fix carbon	Volatiles	Ash	Moisture	Sulfur
Coal quantity	A layer coal rate	B layer coal rate	C layer coal rate	D layer coal rate	E layer coal rate
Air quantity	A layer air rate	B layer air rate	C layer air rate	D layer air rate	E layer air rate
	Total primary air volume			Total secondary air volume	
Injection	Angle of lower injection swing			Angle of middle injection swing	

Once the networks are constructed, the prepared dataset was input into the model. The convergence of the model was determined by monitoring the network's loss during the iteration process. The loss curves of the discriminator and generator networks are shown in Figure 13. Taking 0 as the baseline, the loss curves gradually decline with the increasing number of iteration steps. The loss reaches near-zero levels around 6000 steps, indicating good convergence of the training results.

In addition to the loss function, the generated mode distribution map from the generator network is used as input to the discriminator network, which calculates the probability D(G(z)) of the generated distribution matching the real mode distribution samples corresponding to the operating conditions. Additionally, the probability obtained by inputting real mode distribution samples into the discriminator network is denoted as D(x). Based on the principles of game theory, these probabilities compete with each other. When the generated mode distribution closely matches the real mode distribution of the operating conditions, indicating high accuracy in the generated mode distribution map, the probabilities of D(x) and D (G(z)) become close to each other and fluctuate around .5. As shown in Figure 14, when the training steps exceed 10,000, the probability distributions of D(x) and D(G(z)) stabilize and fluctuate around .5.

3.3.3. *POD-cDCGAN generation results analysis*

By establishing the correlation between the operating data and POD modes, a combined POD-cDCGAN model is created for generating physical fields under arbitrary operating conditions. The trained cDCGAN model is used to validate the generation and reconstruction of physical fields, comparing the reconstructed results with the numerical simulation fields. Five random operating conditions were selected from the production and operational data of the boiler for the validation of the reconstruction results of the physical fields. The operating condition parameters are shown in Table 7. For ease of expression, Load 4 was chosen for qualitative analysis.

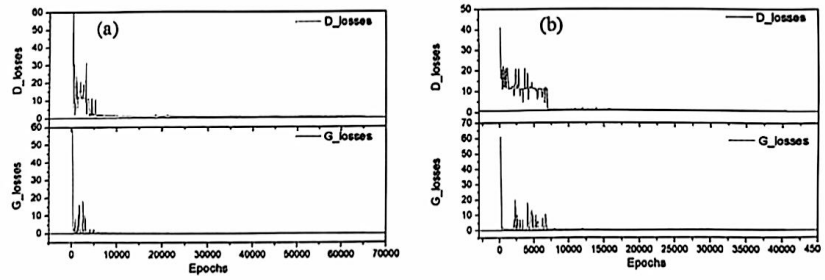

Figure 13. Convergence diagram of loss function: (a) temperature; (b) velocity.

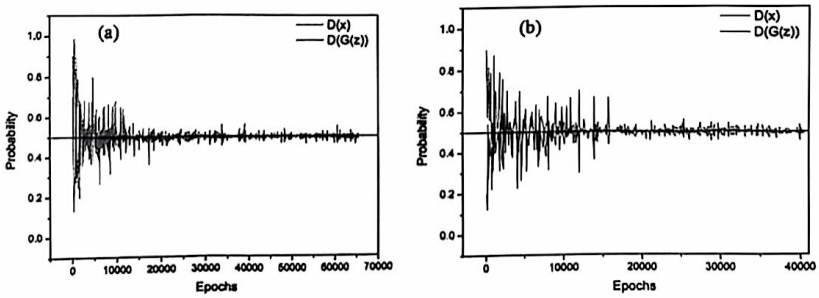

Figure 14. Probability curves of D(x) and D(G(z)): (a) Temperature; (b) velocity.

Table 7. Randomly selected boiler operating conditions.

Boiler operating condition	Load1	Load2	Load3	Load4	Load5
Total moisture (%)	18.74	18.28	18.16	17.46	16.40
Moisture content (%)	2.77	3.58	3.46	3.21	2.10
Ash content (%)	12.49	12.18	11.63	12.45	15.27
Volatile matter (%)	25.62	26.01	25.47	25.64	25.63
Fixed carbon (%)	43.15	43.53	44.74	44.45	42.70
Sulfur content (%)	0.35	0.35	0.43	0.35	0.44
Low calorific value (MJ/kg)	19.88	20.34	20.45	20.96	20.61
A layer coal rate(kg/s)	36.928	32.563	30.708	34.369	28.684
B layer coal rate(kg/s)	36.879	31.332	29.644	33.104	28.504
C layer coal rate(kg/s)	35.667	32.056	30.606	33.996	28.908
D layer coal rate(kg/s)	35.385	30.835	29.276	32.470	31.354
E layer coal rate(kg/s)	0.025	0.027	0.027	0.027	0.030
A layer air rate(Nm3/h)	56.668	50.624	50.529	52.486	51.185
B layer air rate(Nm3/h)	58.449	52.595	50.616	52.563	49.838
C layer air rate(Nm3/h)	57.354	54.776	52.570	57.080	48.239
D layer air rate(Nm3/h)	48.111	45.866	44.377	46.617	48.097
E layer air rate(Nm3/h)	35.343	32.571	32.063	32.061	30.831
Total primary air volume(Nm3/h)	317.102	314.912	312.372	316.370	252.802
Total secondary air volume(Nm3/h)	590.297	530.532	534.604	564.519	515.834
Lower injection swing average angle(%)	54.219	49.516	49.562	54.186	40.578
Middle injection swing average angle(%)	55.571	50.039	50.015	55.674	39.867

Due to the direct impact of burner layers and nozzle layers on the combustion field inside the furnace, where turbulent combustion and chemical reactions are most intense, special attention is given to the physical field distribution of each nozzle layer in the boiler's burner. The generated results for this operating condition are shown in Figure 15.

In Figure 15, it is evident that in the lower group of burners, namely AA, A, AB, B, BC, C, and CC, the temperature field generated by the POD-cDCGAN model exhibits a distinct slanted diamond-shaped distribution. The central region of this distribution manifests lower temperatures, while the surrounding areas display elevated temperatures. Furthermore, with increasing height, the central region gradually diminishes in size, while the high-temperature regions near the walls expand and interconnect.

In the middle and upper group of burners, consisting of DD, D, DE, E, EE, SOFA1, SOFA2, SOFA3, and SOFA4, the temperature field generated by the POD-cDCGAN model demonstrates a continued reduction in the size of the low-temperature central region, accompanied by an overall temperature rise. The highest temperature recorded within this region ranges from 1800–1900K. Notably, the high-temperature zones in the SOFA combustion air region coalesce, suggesting a re-ignition of fuel in that specific area.

By employing the POD-cDCGAN approach, it becomes possible to construct and reconstruct temperature field distributions of varying burner height cross-sections within the tangentially fired boiler (Figure 15 (b)). The resulting reconstructions faithfully restore the inclined diamond-shaped structure observed in different burner height layers. However, there is some deviation in the DD layer and EE layer due to the model input parameters and the complexity of the field distribution in these positions. To simplify the complexity of the model and the difficulty of convergence, the secondary air injections at each layer were not selected as input parameters. This, to some extent, reduces the correlation of the distribution in the secondary air layer and weakens the accuracy of reconstruction. Additionally, these positions are susceptible to the influence of airflow from the lower or upper burner groups, resulting in complex cross-section distributions. Consequently, the reconstructed physical field exhibits some differences in these positions.

Furthermore, the morphology and structure of both high-temperature and low-temperature regions closely align with the temperature field distributions obtained through the Computational Fluid Dynamics (CFD) method (Figure 15 (a)). The distinct high-temperature regions in each layer and the clearly defined inflow from the four corners are accurately represented, ensuring the integrity of their morphological characteristics.

Figure 16 represents the comparison between the velocity fields generated by the POD-cDCGAN combined method and the velocity field distributions obtained through Computational Fluid Dynamics (CFD) simulations. In Figure 16 (b), the cross-sectional velocity field distributions at different heights of the burners are depicted. The inflow from the four corners forms a spindle-shaped pattern, exhibiting good reconstruction of the inflow angle and tangential distribution. The development of the inflow, extending and spreading in the downstream direction, is clearly evident.

Comparing the generated inflow structure by the POD-cDCGAN method with the CFD simulation velocity field in Figure 16 (a), it can be observed that the inflow structures are similar, with consistent distribution of high-velocity regions. The inflow patterns formed in the lower and middle burner area resemble circular shapes, while the phenomenon of shortened inflow in the upper region of the fuel-lean layer and the distribution of the downstream flow direction are in basic agreement.

By qualitatively comparing the generated temperature and velocity field distributions, it can be concluded that the POD-cDCGAN combined method demonstrates the feasibility of rapid reconstruction for scalar and vector fields. The distribution and peak values of the high-temperature and low-temperature regions in the scalar field, represented by temperature, are consistent with the CFD simulation results. Similarly, the inflow structure and development direction of the vector field, represented by velocity, exhibit similarities with the CFD simulation results.

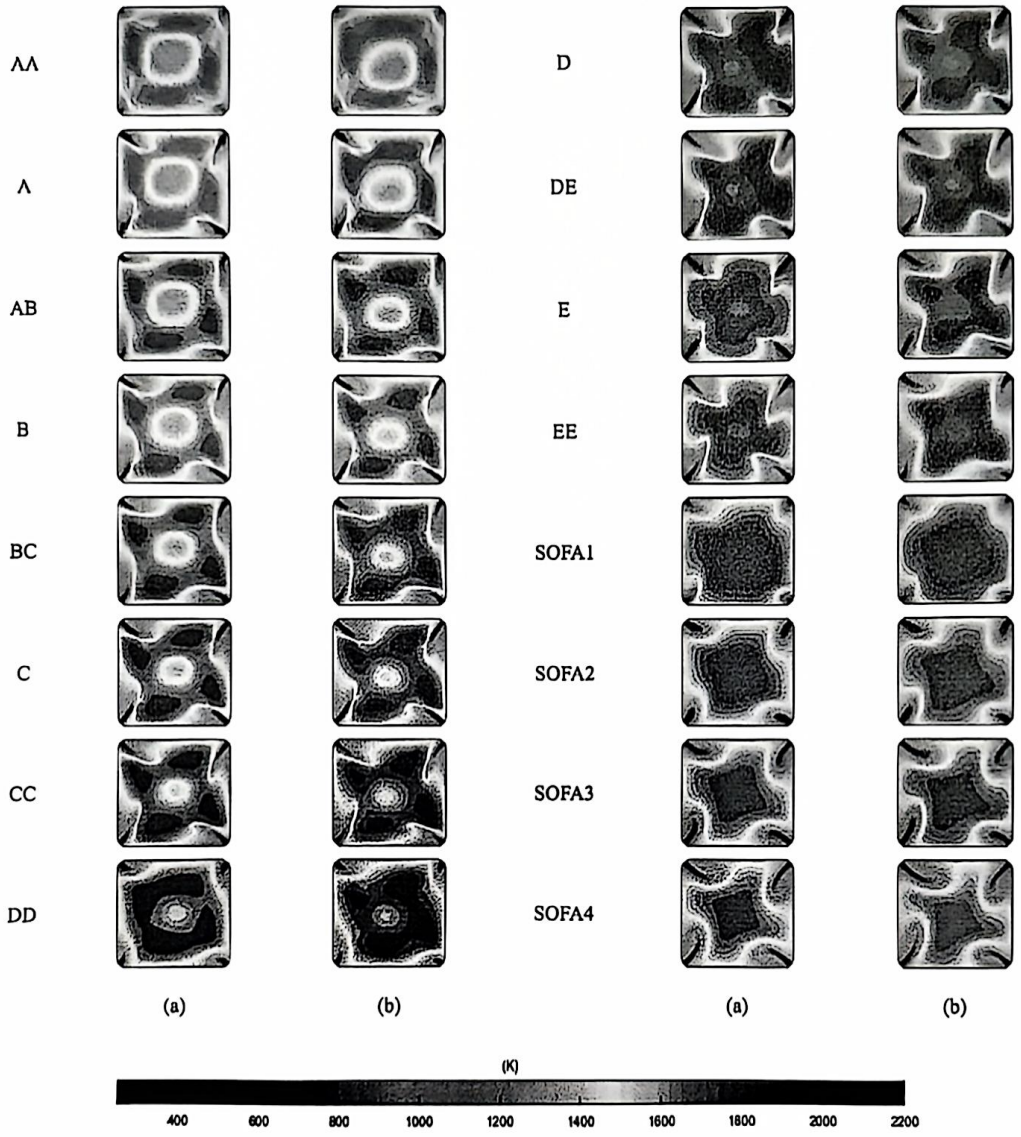

Figure 15. Comparison between generated images and numerical simulation temperature field: (a) numerical simulation field, (b) POD-cDCGAN field.

Performing error analysis between the temperature and velocity field parameters generated by the POD-cDCGAN model and obtained through CFD numerical simulations for these five operating conditions in Table 7. The calculation results for MRE and RRSE are shown in the following Table 8. It can be observed that the temperature and velocity field parameters generated by the POD-cDCGAN model for all grid points exhibit a low average relative error (MRE), staying within a range of 1.5%. This indicates that the POD-cDCGAN-generated field aligns well with the CFD numerical simulation field in terms of numerical consistency, and the generated temperature and velocity fields demonstrate good overall conservation. Additionally, in terms of RRSE, which measures the cumulative effect of the distance between each grid point parameter of the POD-cDCGAN-generated field and the corresponding grid point parameter of the CFD numerical simulation field, the RRSE reflects the specific error magnitude at each grid point. By comparing each grid point, the RRSE for the temperature field distribution generated by POD-cDCGAN is below 6%, and the RRSE for the velocity field distribution has an error below 4.42%.

The POD-cDCGAN model demonstrates reliability and accuracy in generating the physical field of the tangentially fired boiler, both qualitatively and quantitatively. Moreover, the method's efficiency in generating the field has been tested in multiple cases, as shown in Figure 17. The experiments were conducted on computing resources such as Intel XEON E5-2630V4 CPU and NVIDIA GeForce RTX 2080 Ti GPU. After conducting 30 random trials which based on the onsite data of boiler operation, it was found that the POD-cDCGAN model took an average of 10.57 secs to generate the physical field, while the CFD numerical simulation took an average of 101,606 secs (about 28.2 hours). Therefore, the POD-cDCGAN model achieves significantly faster generation of the physical field compared to CFD numerical simulations. With

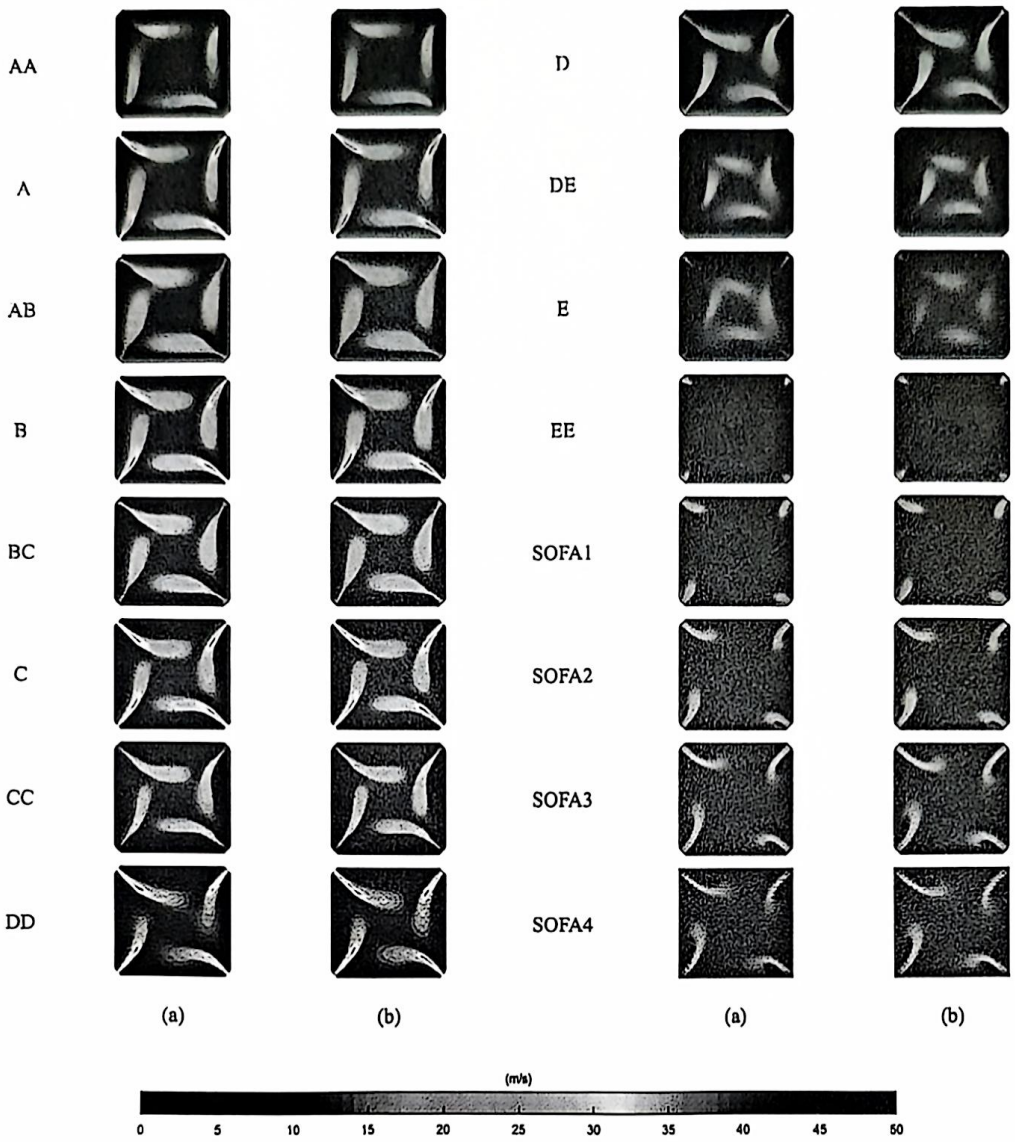

Figure 16. Comparison between generated images and numerical simulation velocity field: (a) numerical simulation field, (b) POD-cDCGAN field.

Table 8. POD-cDCGAN model physical field generates errors.

Operating condition		Load 1	Load 2	Load 3	Load 4	Load 5
Temperature	MRE	0.771	1.456	0.046	−0.165	−1.005
	RRSE	4.109	5.690	5.588	5.061	5.184
Velocity	MRE	−0.198	0.738	−0.908	0.139	0.373
	RRSE	4.011	3.900	4.420	3.794	4.060

accuracy ensured, this enables shorter time for obtaining the field distribution, thereby providing operational guidance for the physical field calculations in practical production operations.

4. Conclusion

In this work, a fast generation method for the physical field of a square-cornered circular coal-fired boiler is proposed using a combination of POD-cDCGAN coupled with simulation data. The conclusions can be summarized as follows:

(1) Numerical simulations of the boiler's typical operating conditions are conducted using CFD methods. Based on this foundation, the POD method was used to reduce the dimensionality of the numerical temperature and velocity fields and extract a series of POD basis functions to characterize the physical fields.
(2) A POD-cDCGAN model was constructed for generating the temperature and velocity fields of the boiler. The model achieved full convergence after 10,000 training steps. The generated temperature and velocity fields exhibited clear and complete inflow patterns, consistent

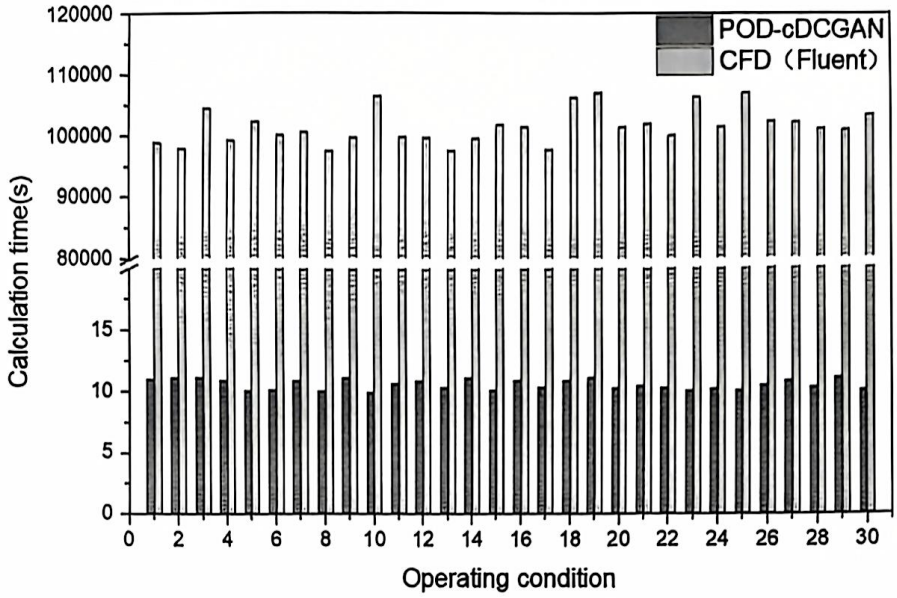

Figure 17. Calculation time of physical field of tangential boiler.

expansion of wake flows, and similar distributions of high-temperature regions. The MRE are all below 1.5%, and the RRSE errors were below 5.7%. In future work, it is possible to enhance the accuracy of the model by adding each secondary air injections parameter as input.

(3) The POD-cDCGAN method provided accurate and rapid generation of the temperature and velocity fields of the boiler, with significantly shorter computation time compared to traditional CFD simulations, while maintaining the accuracy of the physical field distribution. This makes the calculation of the physical field suitable for real-time operation processes, providing an operating reference for boiler operation and tool for the digital twin of tangentially coal-fired boilers.

Nomenclature

Abbreviations

POD	Proper Orthogonal Decomposition
CFD	Computational Fluid Dynamics
AA	AA layer of auxiliary air
AB	AB oil auxiliary air
BC	BC oil auxiliary air
CC	CC layer of auxiliary air
D	D layer of primary air
E	E layer of primary air
SOFA1	Separate over fire air 1
SOFA3	Separate over fire air 3
MRE	Mean relative error
cDCGAN	Conditional Deep Convolutional Generative Adversarial Networks
DCS	Distributed Control System
A	A layer of primary air
B	B layer of primary air
C	C layer of primary air
DD	DD layer of auxiliary air
DE	DE oil auxiliary air
EE	EE layer of auxiliary air
SOFA2	Separate over fire air 2
SOFA4	Separate over fire air 4
RRSE	Root relative squared error

Symbol

G^*	Generator network
M_{ar}	Moisture as received coal
V_{ar}	Volatiles as received coal
$Q_{ar,net}$	Lower heating value as received coal
H_{ar}	Hydrogen content as received coal
N_{ar}	Nitrogen content as received coal
D^*	Discriminator network
A_{ar}	Ash as received coal
$F_{c,ar}$	Fixed carbon as received coal
C_{ar}	Carbon content as received coal
O_{ar}	Oxygen content as received coal
S_{ar}	Sulfur content as received coal

Acknowledgements

The research was supported by the National Natural Science Foundation of China (No. 51976064), and Guangdong Basic and Applied Basic Research Foundation (2022A1515010709). We also acknowledge the support from the Fundamental Research Funds for the Central Universities (2022ZFJH04) and Guangdong Province Key Laboratory of Efficient and Clean Energy Utilization (2013A061401005).

Disclosure statement

No potential conflict of interest was reported by the author(s).

Funding

The work was supported by the Guangdong Basic and Applied Basic Research Foundation [2022A1515010709]; Fundamental Research

Funds for Central Universities [2022ZFJH04]; Guangdong Key Laboratory of Efficient and Clean Energy Utilization [2013A061401005]; National Natural Science Foundation of China [No. 51976064].

ORCID

Youcai Liang http://orcid.org/0000-0002-0671-2952

References

Belosevic, S., M. Sijercic, N. Crnomarkovic, B. Stankovic, and D. Tucakovic. 2009. Numerical prediction of pulverized coal flame in utility boiler furnaces. *ENERGY & FUELS* 23 (11):5401–5412. doi:10.1021/ef9005737.

Bianco, V., M. Szubel, B. Matras, M. Filipowicz, K. Papis, and S. Podlasek. 2021. Cfd analysis and design optimization of an air manifold for a biomass boiler. *Renewable Energy* 163:2018–28. doi:10.1016/j.renene.2020.10.107.

Cao, X., Q. Wang, H. Li, and H. Ma. 2023. Research on fast cfd simulation of automobile flow field based on artificial intelligence. *Journal of Physics: Conference Series* 2441 (1):12011. doi:10.1088/1742-6596/2441/1/012011.

Crnomarkovic, N., S. Belosevic, I. Tomanovic, and A. Milicevic. 2020. New application method of the zonal model for simulations of pulverized coal-fired furnaces based on correction of total exchange areas. *International Journal of Heat and Mass Transfer* 149:119192. doi:10.1016/j.ijheatmasstransfer.2019.119192.

Deng, Z., C. He, Y. Liu, and K. C. Kim. 2019. Super-resolution reconstruction of turbulent velocity fields using a generative adversarial network-based artificial intelligence framework. *PHYSICS OF FLUIDS 31* 31 (12):12. doi:10.1063/1.5127031.

Dewi, C., R. Chen, Y. Liu, and S. Tai. 2022. Synthetic data generation using dcgan for improved traffic sign recognition. *Neural Computing and Applications* 34 (24):21465–21480. doi:10.1007/s00521-021-05982-z.

Diederich, M., L. Di Bartolo, and A. C. Benim. 2023. Comparison of prediction accuracy between interpolation and artificial intelligence application of cfd data for 3d cavity flow. 10.1007/978-981-19-7272-0_35):509-519.

Golgiyaz, S., M. F. Talu, and C. Onat. 2019. Artificial neural network regression model to predict flue gas temperature and emissions with the spectral norm of flame image. *Fuel* 255:115827. doi:10.1016/j.fuel.2019.115827.

Hao, X., P. Xu, H. Suo, and L. Guo. 2020. Numerical investigation of flow and heat transfer of supercritical water in the water-cooled wall tube. *International Journal of Heat and Mass Transfer* 148:119084. doi:10.1016/j.ijheatmasstransfer.2019.119084.

Jiang, W., T. Pan, G. Jiang, Z. Sun, H. Liu, Z. Zhou, B. Ruan, K. Yang, and X. Gao. 2023. Data-driven physical fields reconstruction of supercritical-pressure flow in regenerative cooling channel using pod-ae reduced-order model. *International Journal of Heat and Mass Transfer* 217:124699. doi:10.1016/j.ijheatmasstransfer.2023.124699.

Kang, Z., and X. Ding. 2020. Numerical analysis on combustion process and sodium transformation behavior in a 660 mw supercritical face-fired boiler purely burning high sodium content zhundong coal. *Journal of the Energy Institute* 93 (2):450–462. doi:10.1016/j.joei.2019.07.006.

Lee, W., K. Jang, W. Han, and K. Y. Huh. 2021. Model order reduction by proper orthogonal decomposition for a 500 mwe tangentially fired pulverized coal boiler. *Case Studies in Thermal Engineering* 28:101414. doi:10.1016/j.csite.2021.101414.

Li, G., Y. Li, C. Fang, J. Su, H. Wang, S. Sun, G. Zhang, and J. Shi. 2023. Research on fault diagnosis of supercharged boiler with limited data based on few-shot learning. *Energy* 281 (10):128286. doi:10.1016/j.energy.2023.128286.

Li, H., G. Li, L. Lin, H. Yu, and Y. Yu. 2019. Context-aware semantic inpainting. *IEEE Transactions on Cybernetics* 49 (12):4398–4411. doi:10.1109/TCYB.2018.2865036.

Liu, J., F. Hou, L. Zhang, C. Duan, H. Liu, X. Zhang, Z. Hu, and X. Yang. 2022. Experimental study on optimal adjustment of scr ammonia injection for 1000 mw coal-fired unit based on multi-field cooperative diagnosis. 10.1007/978-981-16-1657-0_58):763-777.

Liu, G., W. Hu, S. Hao, C. Gao, Y. Liu, W. Wu, and L. Li. 2024. A fast computational method for internal temperature field in oil-immersed power transformers. *Applied Thermal Engineering* 236:121558. doi:10.1016/j.applthermaleng.2023.121558.

Lou, C., and H. Zhou. 2005. Deduction of the two-dimensional distribution of temperature in a cross section of a boiler furnace from images of flame radiation. *Combustion and Flame* 143 (1):97–105. doi:10.1016/j.combustflame.2005.05.005.

Madejski, P., N. Modliński, M. Pronobis, B. Hernik, and K. Jagodzińska. 2019. Numerical investigation using two different cfd codes of pulverized-coal combustion process characteristic in an industrial power plant boiler. E3S Web of Conferences 82:1009. 10.1051/e3sconf/20198201009.

Meng, Y., X. Wu, J. Oladejo, X. Dong, Z. Zhang, J. Deng, Y. Yan, H. Zhao, E. Lester, T. Wu, et al. 2021. Application of machine learning in industrial boilers: fault detection, diagnosis, and prognosis. *ChemBioeng Reviews* 8 (5):535–44. doi:10.1002/cben.202100008.

Milićević, A., S. Belošević, N. Crnomarković, I. Tomanović, and D. Tucaković. 2020. Mathematical modelling and optimisation of lignite and wheat straw co-combustion in 350 mwe boiler furnace. *Applied Energy* 260:114206. doi:10.1016/j.apenergy.2019.114206.

Mitchell, E. J. S., A. R. Lea-Langton, J. M. Jones, A. Williams, P. Layden, and R. Johnson. 2016. The impact of fuel properties on the emissions from the combustion of biomass and other solid fuels in a fixed bed domestic stove. *Fuel Processing Technology* 142:115–123. doi:10.1016/j.fuproc.2015.09.031.

Modliński, N., P. Madejski, T. Janda, K. Szczepanek, and W. Kordylewski. 2015. A validation of computational fluid dynamics temperature distribution prediction in a pulverized coal boiler with acoustic temperature measurement. *Energy* 92:77–86. doi:10.1016/j.energy.2015.05.124.

Park, J., W. Lee, and K. Y. Huh. 2022. Model order reduction by radial basis function network for sparse reconstruction of an industrial natural gas boiler. *Case Studies in Thermal Engineering* 37:102288. doi:10.1016/j.csite.2022.102288.

Patgiri, R., A. Biswas, and P. Roy. 2021. *Medical image generation using generative adversarial networks: A review*. In Singapore: Springer Singapore Pte. Limited.

Purnomo, F., A. Setiyawan, Suwarno, V. Djanali, F. Mubarok, and B. Pramujati. 2019. Numerical study on in-furnace blending coal combustion characteristics in a 625 mw tangentially fired pulverized coal boiler. *AIP Conference Proceedings* 2187 (1). doi: 10.1063/1.5138293.

Purnomo, H., B. Sudarmanta, Suwarno, V. Djanali, F. Mubarok, and B. Pramujati. 2019. Numerical simulation of coal particle size (fineness) effect to combustion characteristics of sub-critical pulverized coal boiler 600 mw capacity. *AIP Conference Proceedings* 2187 (1). doi: 10.1063/1.5138288.

Qian, G., and J. Liu. 2022. Fault diagnosis based on conditional generative adversarial networks in nuclear power plants. *Annals of Nuclear Energy* 176:109267. doi:10.1016/j.anucene.2022.109267.

Qinghong, W. 2020. Computer image processing and neural network technology for boiler thermal energy diagnosis. *Thermal Science* 24 (5B):3221–28. doi:10.2298/TSCI191121113Z.

Radford, A., L. Metz, and S. Chintala. 2015. Unsupervised representation learning with deep convolutional generative adversarial networks. *arXiv preprint arXiv* 1511.06434.

Rajabi, M. M., P. Komeilian, X. Wan, and R. Farmani. 2023. Leak detection and localization in water distribution networks using conditional deep convolutional generative adversarial networks. *Water Research* 238:120012. doi:10.1016/j.watres.2023.120012.

Ronquillo-Lomelí, G., and A. García-Moreno. 2024. A machine learning-based approach for flames classification in industrial heavy oil-fire boilers. *Expert Systems with Applications* 238:122188. doi:10.1016/j.eswa.2023.122188.

Salinas, C. T., Y. Pu, C. Lou, and D. B. Dos Santos. 2020. Experiments for combustion temperature measurements in a sugarcane bagasse large-scale boiler furnace. *Applied Thermal Engineering* 175:115433. doi:10.1016/j.applthermaleng.2020.115433.

Sha, J., X. Chen, Y. Chang, M. Zhang, and X. Li. 2023. A spatial weather generator based on conditional deep convolution generative adversarial nets (cdcgan). *Climate Dynamics* 62 (2):1275–90. doi:10.1007/s00382-023-06971-9.

Sung, Y., C. Moon, S. Eom, G. Choi, and D. Kim. 2016. Coal-particle size effects on no reduction and burnout characteristics with air-staged combustion in a pulverized coal-fired furnace. *Fuel* 182:558–567. doi:10.1016/j.fuel.2016.05.122.

Sun, F., A. Huang, Z. Wu, W. Huang, and M. Zhang. 2022. A fast reconstruction method for temperature field based on principal component analysis and convolutional autoencoder. 2022 IEEE International Symposium on Product Compliance Engineering - Asia (ISPCE-ASIA), Guangzhou, Guangdong Province, China, 1–5.

Wang, X., H. Chen, U. Sultan, X. Zhu, Z. Wang, and G. Xiao. 2019. A brief review of the combustion diagnosing techniques for coal-fired boilers of power plants in china. *IEEE Access* 7:126127–126136. doi:10.1109/ACCESS.2019.2939359.

Wang, T., X. Chen, and W. Zhong. 2024. Air distribution and coal blending optimization to reduce slagging on coal-fired boiler water wall based on pod reduced order modeling for cfd. *Fuel* 357:129856. doi:10.1016/j.fuel.2023.129856.

Wang, H., C. Zhang, and X. Liu. 2020. Heat transfer calculation methods in three-dimensional cfd model for pulverized coal-fired boilers. *Applied Thermal Engineering* 166:114633. doi:10.1016/j.applthermaleng.2019.114633.

Wang, H., X. Zhou, Q. Yang, J. Chen, C. Dong, and L. Zhao. 2021. A reconstruction method of boiler furnace temperature distribution based on acoustic measurement. *IEEE Transactions on Instrumentation and Measurement* 70:1–13. doi:10.1109/TIM.2021.3123218.

Yan, L., B. He, F. Yao, R. Yang, X. Pei, C. Wang, and J. Song. 2012. Numerical simulation of a 600 mw utility boiler with different tangential arrangements of burners. *ENERGY & FUELS* 26 (9):5491–5502. doi:10.1021/ef300929v.

Yan, W., K. Li, X. Huang, L. Yu, C. Lou, and Y. Chen. 2020. Online measurement of the flame temperature and emissivity during biomass volatile combustion using spectral thermometry and image thermometry. *Energy & Fuels* 34 (1):907–919. doi:10.1021/acs.energyfuels.9b03188.

Ye, T., M. Dong, Y. Liang, J. Long, W. Li, and J. Lu. 2022. Modeling and optimization of the nox generation characteristics of the coal-fired boiler based on interpretable machine learning algorithm. *International Journal of Green Energy* 19 (5):529–543. doi:10.1080/15435075.2021.1947827.

Ye, T., M. Dong, J. Long, Y. Zheng, Y. Liang, and J. Lu. 2022. Multi-objective modeling of boiler combustion based on feature fusion and bayesian optimization. *Computers & Chemical Engineering* 165:107913. doi:10.1016/j.compchemeng.2022.107913.

Yu, G., J. Sang, and Y. Sun. 2020. Thermal energy diagnosis of boiler plant by computer image processing and neural network technology. *Thermal Science* 24 (5 Part B):3367–3374. doi:10.2298/TSCI191218128Y.

Zhan, F., G. Ding, and D. Zhuang. 2020. Numerical model of particle deposition on wet fin surfaces of heat exchanger under dehumidifying conditions. *International Journal of Heat and Mass Transfer* 149:119258. doi:10.1016/j.ijheatmasstransfer.2019.119258.

Zhang, S., G. Shen, L. An, and Y. Niu. 2015. Online monitoring of the two-dimensional temperature field in a boiler furnace based on acoustic computed tomography. *Applied Thermal Engineering* 75:958–966. doi:10.1016/j.applthermaleng.2014.10.085.

Zhong, Z., A. Y. Sun, H. Jeong, and A. T. U. S. Univ. Of Texas. 2019. Predicting co2 plume migration in heterogeneous formations using conditional deep convolutional generative adversarial network. *Water Resources Research* 55 (7):5830–51. doi:10.1029/2018WR024592.

Zhong, Z., A. Y. Sun, Y. Wang, and B. Ren. 2020. Predicting field production rates for waterflooding using a machine learning-based proxy model. *Journal of Petroleum Science & Engineering* 194:107574. doi:10.1016/j.petrol.2020.107574.

Zhou, A., H. Xu, M. Xu, W. Yu, Z. Li, and W. Yang. 2020. Numerical investigation of biomass co-combustion with methane for nox reduction. *Energy* 194:116868. doi:10.1016/j.energy.2019.116868.

Zhu, X., and Y. Ji. 2023. A reduced order model based on adaptive proper orthogonal decomposition incorporated with modal coefficient learning for digital twin in process industry. *Journal of Manufacturing Processes* 102:780–94. doi:10.1016/j.jmapro.2023.07.061.